



Communication

The Synthesis of Manganese Hydroxide Nanowire Arrays for a High-Performance Zinc-Ion Battery

Jiangfeng Gong^{1,*}, Bingxin Zhu¹, Zhupeng Zhang¹, Yuanyuan Xiang¹, Chunmei Tang^{1,*}, Qingping Ding² 
and Xiang Wu^{3,*} 

¹ College of Science, Department of Physics, Hohai University, Nanjing 210098, China;

zhubingxin20211226@163.com (B.Z.); zzp18752006001@163.com (Z.Z.); yyxiang@hhu.edu.cn (Y.X.)

² Ames Laboratory, Department of Physics and Astronomy, Iowa State University, Ames, IA 50011, USA; qingping.ding@gmail.com

³ School of Materials Science and Engineering, Shenyang University of Technology, Shenyang 110870, China

* Correspondence: jfgong@hhu.edu.cn (J.G.); cmtang@hhu.edu.cn (C.T.); wuxiang05@sut.edu.cn (X.W.)

Abstract: The morphology, microstructure as well as the orientation of cathodic materials are the key issues when preparing high-performance aqueous zinc-ion batteries (ZIBs). In this paper, binder-free electrode Mn(OH)₂ nanowire arrays were facilely synthesized via electrodeposition. The nanowires were aligned vertically on a carbon cloth. The as-prepared Mn(OH)₂ nanowire arrays were used as cathode to fabricate rechargeable ZIBs. The vertically aligned configuration is beneficial to electron transport and the free space between the nanowires can provide more ion-diffusion pathways. As a result, Mn(OH)₂ nanowire arrays yield a high specific capacitance of 146.3 Ma h g⁻¹ at a current density of 0.5 A g⁻¹. They also demonstrates ultra-high diffusion coefficients of 4.5 × 10⁻⁸~1.0 × 10⁻⁹ cm² s⁻¹ during charging and 1.0 × 10⁻⁹~2.7 × 10⁻¹¹ cm² s⁻¹ during discharging processes, which are one or two orders of magnitude higher than what is reported in the studies. Furthermore, the rechargeable Zn//Mn(OH)₂ battery presents a good capacity retention of 61.1% of the initial value after 400 cycles. This study opens a new avenue to boost the electrochemical kinetics for high-performance aqueous ZIBs.

Keywords: manganese hydroxide; aqueous zinc-ion battery; surfactant assistant; electrodeposition



Citation: Gong, J.; Zhu, B.; Zhang, Z.; Xiang, Y.; Tang, C.; Ding, Q.; Wu, X.

The Synthesis of Manganese

Hydroxide Nanowire Arrays for a High-Performance Zinc-Ion Battery.

Nanomaterials **2022**, *12*, 2514. <https://doi.org/10.3390/nano12152514>

Academic Editors: Sergio Brutti and Cheol-Min Park

Received: 7 July 2022

Accepted: 19 July 2022

Published: 22 July 2022

Publisher's Note: MDPI stays neutral with regard to jurisdictional claims in published maps and institutional affiliations.



Copyright: © 2022 by the authors. Licensee MDPI, Basel, Switzerland. This article is an open access article distributed under the terms and conditions of the Creative Commons Attribution (CC BY) license (<https://creativecommons.org/licenses/by/4.0/>).

1. Introduction

With the growing environmental concerns, the development of rechargeable batteries with high electrochemical energy storage technology is highly needed to meet the requirements of renewable and sustainable energy storage, such as wind or solar power. Lithium-ion batteries (LIBs) are considered as the most promising power sources for their superior cycle performance and high-energy density [1,2]. Although LIBs have been commercialized, some crucial problems, such as high price, low power density and safety concerns, still exist [3,4]. Aqueous rechargeable batteries focused on multivalent metal particles were extensively studied to resolve these drawbacks due to their high safety (aqueous electrolytes) and energy (multi-purpose transporters) efficiencies. The renaissance of aqueous zinc-ion batteries (ZIBs) shows encouraging choices for next-generation energy storage devices for their excellent safety and environmental aspects [5–8], along with other advantages of low cost, low redox potential and high capacity of the Zn anode.

It is a system engineered to promote the development of ZIBs with great commercial prospects. To improve the intrinsic safety of ZIBs, some scientists are devoted to suppressing the growth of zinc dendrites [9–11]. Current research efforts are mainly focused on exploring high-performance cathode materials of ZIBs, such as manganese-based [12–19] and vanadium-based materials [20,21], and so on [22–25]. Manganese-based oxides are the most favorable cathode materials for aqueous ZIBs because of these advantages. First, a

manganese ion consists of various oxidation states (Mn^{2+} , Mn^{3+} , Mn^{4+}); MnO_2 can accommodate one Zn^{2+} insertion per formula with a high theoretical capacity of approximately 616 mA h/g, in which the Mn^{4+} is reduced to Mn^{2+} [14]. Second, MnO_2 exists in various crystal forms. In these structures, the basic structural MnO_6 octahedra units are connected to each other by a co-angle/co-edge, constructing chain, tunnel and layered structures with enough space accommodating foreign cations. The advantages of these structures are the high availability of a Zn^{2+} storage site, increased electrolyte penetration and more favorable surface/interfacial properties [26]. In 2012, Kang's group reported a zinc-ion storage strategy by utilizing $\alpha\text{-MnO}_2$ as an effective cathodic electrode for the first time [27]; since then, manganese-based materials have been widely studied and demonstrated as a compelling candidate material for aqueous ZIBs. For example, Wu et al. reported an aqueous Zn/ MnO_2 battery using $\alpha\text{-MnO}_2$ /graphene scrolls as the cathode material, and the cathode delivered a prominent capacity of 362.2 mA h g^{-1} at a current density of 0.3 A g^{-1} with long-term cyclability [10]. Some other works also show similar results [13,15,26,28]. In such electrochemical systems, the typical chemical conversion reaction mechanism of the cathodic MnO_2 is one electron redox (Mn^{4+} to Mn^{3+}) in the conventional natural aqueous electrolyte: $\text{MnO}_2 + \text{H}^+ + \text{e}^- \leftrightarrow \text{MnOOH}$ [29]. Inspired by this equation, Zhang et al. synthesized $\gamma\text{-MnOOH}$ nanorods that possess an enhanced electrochemical performance with a specific capacity of 965 mA h g^{-1} at a current density of 200 mA g^{-1} for lithium-ion batteries [30]. As a layered material, manganese hydroxide possesses a large interlayer spacing, which provides a rapid transport pathway for efficient Zn^{2+} insertion/extraction. As a matter of fact, there is a vital consideration for choosing suitable manganese hydroxide or transition metal hydroxide hosts as the cathode in ZIBs [31–37]. Binders and conductive carbon are usually used as additives to prepare conventional powder electrodes. The additives may generate “dead volume” due to the bonding process of the active material to the substrate. It is necessary to develop a feasible way to manufacture binder-free cathodes to improve the electrochemical performance of ZIBs.

In this study, binder-free electrode $\text{Mn}(\text{OH})_2$ nanowire arrays are facilely synthesized via electrodeposition. The nanowires were vertically aligned on a carbon cloth. The configuration is beneficial to electron transport during the redox reaction. Meanwhile, the free space between the nanowires may provide more ion diffusion pathways. The as-prepared $\text{Mn}(\text{OH})_2$ nanowire arrays were used as cathodes to fabricate a high-performance rechargeable aqueous ZIBs with 2 M Zn (CF_3SO_3)₂ serving as the electrolyte. As a result, $\text{Mn}(\text{OH})_2$ nanowire arrays yielded a high specific capacitance of 146.3 mA h g^{-1} at a current density of 0.5 A g^{-1} . It also demonstrates ultra-high diffusion coefficients of $4.5 \times 10^{-8} \sim 1.0 \times 10^{-9} \text{ cm}^2 \text{ s}^{-1}$ during charging and $1.0 \times 10^{-9} \sim 2.7 \times 10^{-11} \text{ cm}^2 \text{ s}^{-1}$ during discharging processes, which are one or two orders of magnitude higher than in other reported studies. Furthermore, the rechargeable Zn// $\text{Mn}(\text{OH})_2$ battery presents a good capacity retention of 61.1% of the initial value after 400 cycles. Our work presents an inspiring solution to develop a binder-free electrode with a simple surfactant-assisted electroplate method. This work opens a new avenue to boost the electrochemical kinetics for high-performance aqueous ZIBs.

2. Materials and Methods

2.1. Materials

All raw materials purchased were of analytical grade and were not purified before use. Manganese nitrate $\text{Mn}(\text{NO}_3)_2 \cdot 4\text{H}_2\text{O}$ (CAS No.10377-66-9) was purchased from Nanjing Reagent Co. (Nanjing, China); ethylene glycol (EG, $\text{C}_2\text{H}_6\text{O}_2$, CAS No. 107-21-1), sodium dodecyl sulfate (SDS, $\text{C}_{12}\text{H}_{25}\text{NaO}_4\text{S}$, CAS No. 151-21-3) and absolute ethanol ($\text{C}_2\text{H}_5\text{OH}$, CAS No. 64-17-5) were purchased from Kelong Chemical Reagent Co. (Chengdu, China); and the carbon cloth (CC, HCP330N) and glass-fiber filter paper (Whatman GF/F) were purchased from Guangdong Canrd New Energy Technology Co. (Dongguan, China). All electrolytes were prepared with distilled water.

2.2. Preparation of SDS-Mn(OH)₂ on CC

The electrodeposition of Mn(OH)₂ nanowire arrays was performed under potentiostatic mode with a thermostatic control system. A conventional three-electrode system was used to deposit Mn(OH)₂ nanowire films assisted with SDS confinement. A platinum electrode and standard saturated calomel electrode (SCE) (saturated KCl) were used as counter and reference electrodes, respectively. The carbon cloth (CC) was cut into a circular shape with a diameter of 1.4 cm. After being washed and dried with ethanol and de-ionized water several times, it was used as the working electrode. The plating solution was composed of 5% SDS, 20% EG and 0.05 M Mn(NO₃)₂. The electrochemical deposition was conducted at a voltage of −1.3 V with a temperature of 70 °C for 30 min. Finally, the deposited samples were immersed in ethanol and de-ionized water, in turn, and dried in an oven at 60 °C for 2 h. The mass loading of manganese hydroxide was 2.4 mg cm^{−1}.

2.3. Structural Characterization

The crystal structure of the Mn(OH)₂ nanowire array was analyzed by X-ray diffractometer (XRD, D8 ADVANCE, Bruker, Karlsruhe, Germany). The morphologies and microstructures of the Mn(OH)₂ nanowires were examined by scanning electron microscope (SEM, Gemini 500, Zeiss, Oberkochen, Baden-Württemberg, Germany) and transmission electron microscope (TEM, Tecnai F20, FEI, Hillsborough, OR, USA). The composition of Mn(OH)₂ was characterized by X-ray photoelectron spectroscopy (XPS ESCALAB 250 Xi, Thermo Fisher Scientific, Waltham, MA, USA).

2.4. Fabrication of CC@Mn(OH)₂//Zn Coin Cells

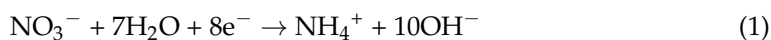
Electrochemical measurements were performed using CR2032 coin-type cells. The cells were assembled using the CC@Mn(OH)₂ composite as cathode, zinc metal foil as anode and glass fiber as the separator. A 2 M Zn(CF₃SO₃)₂ aqueous electrolyte was used as the electrolyte. An electric-pressure battery-sealing machine (MSK-160E) was used to seal the cell; the sealing pressure was kept at 0.600 t. Finally, the encapsulated cells were shelved for 12 h.

2.5. Electrochemical Tests

All tests were measured using the assembled 2032-coin cell. Cyclic voltammetry (CV), electrochemical impedance spectroscopy (EIS) and galvanostatic charge–discharge (GCD) were performed using the electrochemical workstation (CHI660, Chenhua, Shanghai, China). CV was conducted at various scan rates under a voltage window of 0.3–1.8 V. EIS was performed at open-circuit potential in a frequency range from 0.01 Hz to 10 kHz with a perturbation of 5 mV. The rate performance, cycle life and galvanostatic intermittent titration technique (GITT) were studied by using the Neware testing system (CT-4000, Neware, Shenzhen, China).

3. Results and Discussion

The Mn(OH)₂ nanowire arrays were prepared on CC through a facile electrodeposition method, in which SDS was used as a templating agent. The electrodeposition of manganese hydroxide proceeded through the following reactions [38]:



The addition of the surfactant during electrodeposition played a vital role in modifying the structure of Mn(OH)₂ by controlling the nucleation and growth mechanism. By introducing SDS to the electrolyte, the surfactant could be absorbed on the Mn(OH)₂ surface under the electric field force. The interaction between the surfactant and Mn(OH)₂ surface could be controlled in the thin interfacial region by electrochemical deposition; the Mn²⁺ ions were incorporated at the tip of the Mn(OH)₂ coatings forming the nanowire-shaped

morphology as shown in Figure 1a. It can clearly be observed that large wire-shaped nanostructures are vertically aligned on the carbon fiber, with a length more than 5 μm . The enlarged SEM image is also shown in Figure 1b in which the diameter of the nanowire is about 25 nm. In contrast to our present work, without the surfactant of SDS in the electroplating solution, the deposit is a thin film composed of nanosheets [31,32]. It can be concluded that the introduction of SDS changes the morphology and structure during the electrochemical deposition process. Compared with the nanosheets, the vertically aligned $\text{Mn}(\text{OH})_2$ nanowires expose a larger specific surface area and more active sites. This morphology and structure are helpful for the intercalation and de-intercalation of Zn^{2+} . After the deposition, the surfactants can be easily removed from the surface of the nanowires with alcohol. Figure 1c shows the XRD pattern of $\text{Mn}(\text{OH})_2$ (for comparison, the XRD pattern of the CC substrate is also provided). It is obvious that a high amorphous peak centered at 25.52° appears, which comes from the CC substrate. The peaks at $2\theta = 18.97^\circ$ and 36.82° correspond to the (0 0 1) and (0 1 1) planes of $\text{Mn}(\text{OH})_2$ (JCPDS No: 73-1133), respectively.

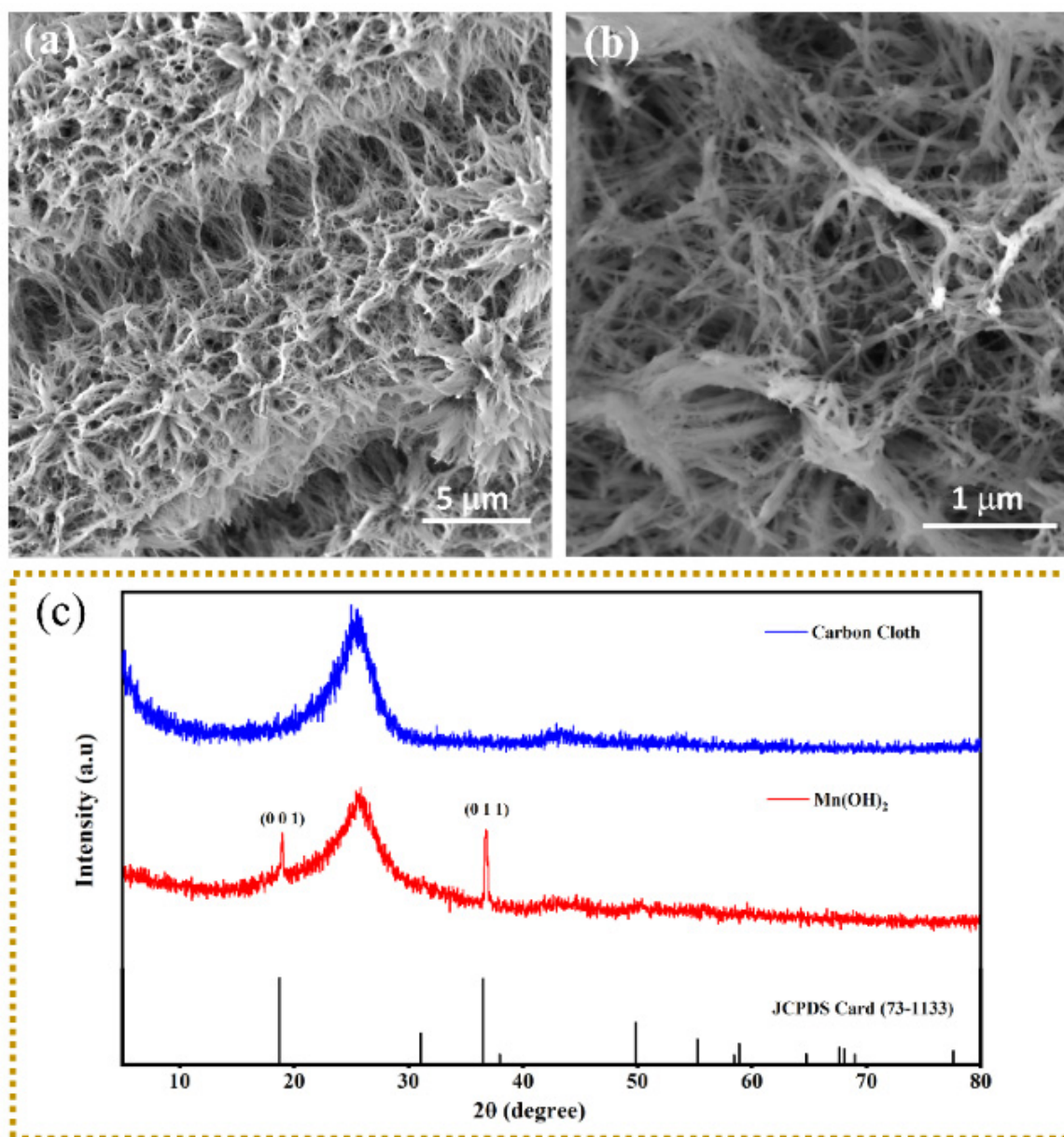


Figure 1. (a,b) SEM images; (c) XRD pattern of as-prepared $\text{Mn}(\text{OH})_2$ nanowire arrays.

The morphology and microstructure of the prepared sample were further investigated by TEM. The loose structure of SDS associated with $\text{Mn}(\text{OH})_2$ nanowires could be verified by the TEM image shown in Figure 2a. Figure 2b shows a high-resolution TEM image of $\text{Mn}(\text{OH})_2$ nanowires and the corresponding selected area electron diffraction (SAED). The SAED pattern presents a periodic structure indicating the single-crystal character of the sample. The high-resolution TEM image shows clear lattice fringes, and the measured d-spacing is 0.515 nm, corresponding to the (001) plane of $\text{Mn}(\text{OH})_2$. Figure 2c shows a typical high-angle annular dark field (HAADF) image of the loose nanowire bunch; the EDS mappings (Figure 2d,e) and spectrum (Figure 2f) were collected from the central rectangular area. Only Mn and O signals can be detected in the EDS and the elements of Mn and O distribute uniformly in the entire scanned area, which reflects that the sample is $\text{Mn}(\text{OH})_2$ indirectly.

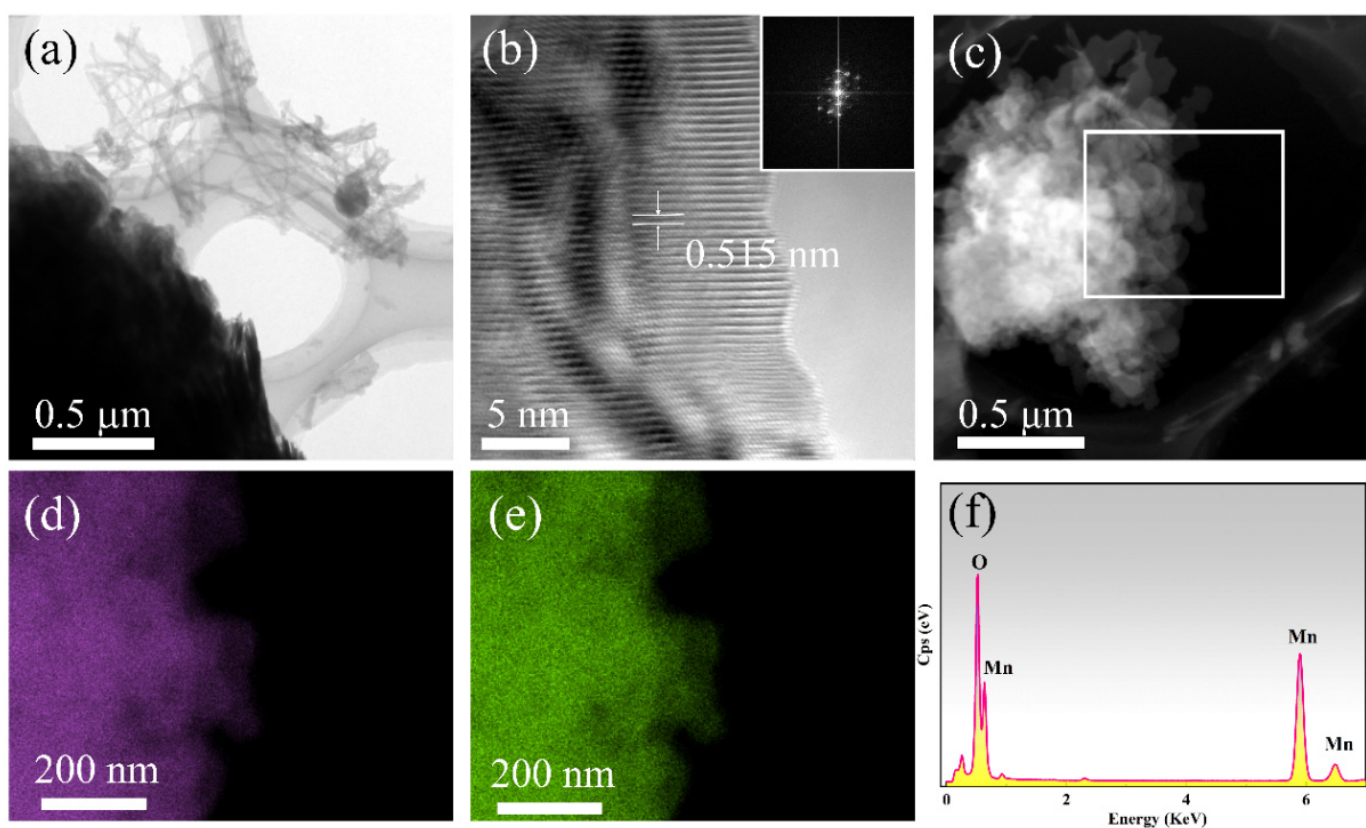


Figure 2. (a) TEM image, (b) HRTEM image and SAED pattern, (c) HAADF image of $\text{Mn}(\text{OH})_2$ nanowires. (d–f) Elemental mappings of Mn and O and EDS spectrum of the products.

XPS was also used to analyze the valence states and chemical composition of the samples. The XPS spectrum shows significant peaks of Mn and O (Figure 3a) indicating that the sample is composed of Mn and O elements, which further confirms that the sample is $\text{Mn}(\text{OH})_2$ (the peak of C is from the carbon cloth substrate). Figure 3b shows the core level spectrum of the Mn 2p state. There are two sets of spin-orbital peaks at the binding energies of 653.3 and 641.9 eV, corresponding to Mn $2p^{1/2}$ and Mn $2p^{3/2}$ spin-orbital peaks [39–41]. The average oxidation state of Mn can also be estimated by the binding energy (ΔE_b) between two Mn 3s peaks. The Mn 3s core-level spectrum in Figure 3c manifests that the peak splitting of the doublet is ≈ 5.7 eV, which is between 5.41 and 6.1 eV for Mn^{3+} and Mn^{2+} , respectively [42]. The estimated average valence state of manganese in the sample is about 2.2, which indicates the partial oxidation of the sample. To evaluate the exact valence of Mn, the O 1s spectrum was also analyzed. The core-level O 1s XPS spectrum can be deconvoluted into three sub-peaks, as show in Figure 3d. Three obvious peaks with binding energies of 530.2, 531.54 and 532.2 eV are assigned to anhydrous manganese oxides

(Mn-O-Mn bond), hydrated manganese oxides (Mn-O-H bond) and residual structure water (H-O-H bond), respectively [40,41]. The presence of Mn-O-H and H-O-H bonds indicates that a large quantity of crystallized water of is embedded in the sample.

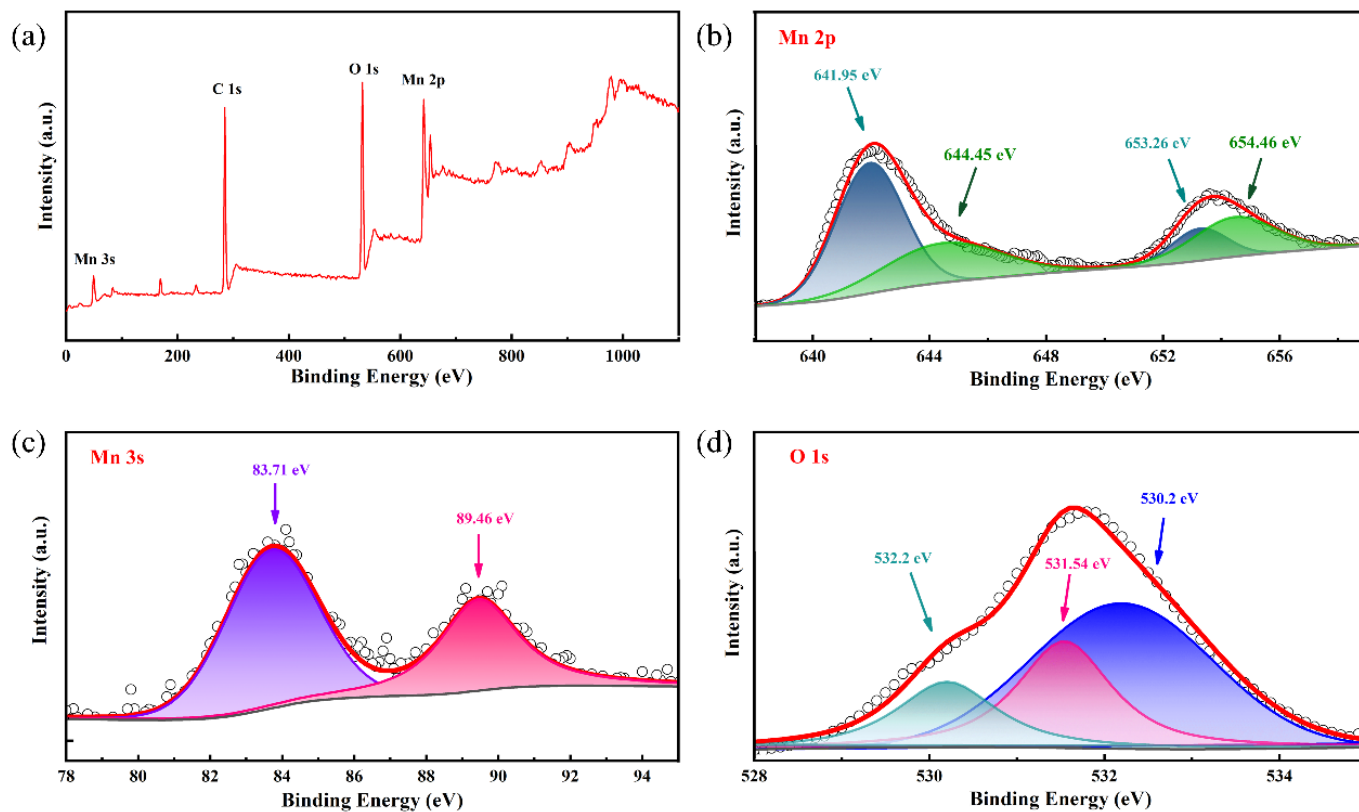


Figure 3. (a) The XPS spectra, (b) Mn 2p, (c) Mn 2s and (d) O 1s core-level XPS spectra of as-prepared Mn(OH)₂ nanowire arrays.

The electrochemical performance of the product was investigated systematically within a typical 2032-coin cell at room temperature. Figure 4a presents the CV curves of Mn(OH)₂ with a scan rate of 1 mV^{-1} in a potential window of 0.3–1.9 V from the first to the third cycle. One oxidation peak and two reduction peaks are obviously observed. The oxidation peak at 1.60 V resulted from the extraction of Zn^{2+} from the cathode material. For the cathodic process, the two-step charge storage was attributed to the different insertion mechanisms, the first cathodic peak located at 1.38 V was attributed to H^+ intercalation, while the second cathodic peak located at 1.13 V was caused by Zn^{2+} intercalation [6]. Obviously, the first cycle was quite different from the last two, which may have been due to the activation process of the battery. However, the last two cycles basically overlapped, which indicated that the electrochemical process of the prepared sample was highly reversible. Figure 4b shows the constant current charge–discharge curves at different current densities from 0.1 to 1.0 Ag^{-1} . It can be observed from the curves that there are two charge–discharge platforms; the first plateau is caused by the Zn^{2+} intercalation and the second plateau is attributed to the H^+ intercalation [6]. The energy density of the SDS-Mn(OH)₂ cathode was 197.6 W h kg^{-1} at a current density of 0.1 Ag^{-1} . The rate performance of the product is shown in Figure 4c. Mn(OH)₂ delivered excellent reversible rate capacities of 146.3, 128.5, 114.2, 101.4, 94.5 and 88.2 Ma h g^{-1} at the current densities of 0.1, 0.2, 0.3, 0.5, 0.7 and 1.0 Ag^{-1} , respectively. The value is comparable to an MnO₂ nanofiber [29], Mn(OH)₂@porous Ni [38], V₂O₅/CNT [21] and PANi [25]. More importantly, when the rate returns to 0.1 Ag^{-1} , the specific capacity of the sample retains 94.8% of the initial capacity, indicating good layer structure stability and excellent electrochemical reversibility. Figure 4d shows the cyclic stability of SDS-Mn(OH)₂ in ZIBs; the discharge capacity retention of the battery

is 61.1% with a coulombic efficiency near 100% at 0.5 Ag^{-1} after 400 charge and discharge cycles, substantiating the impressive durability of the $\text{Mn}(\text{OH})_2$ cathode. The capacity loss may be due to the collapse of the network of nanowires during the cycle (Figure S1).

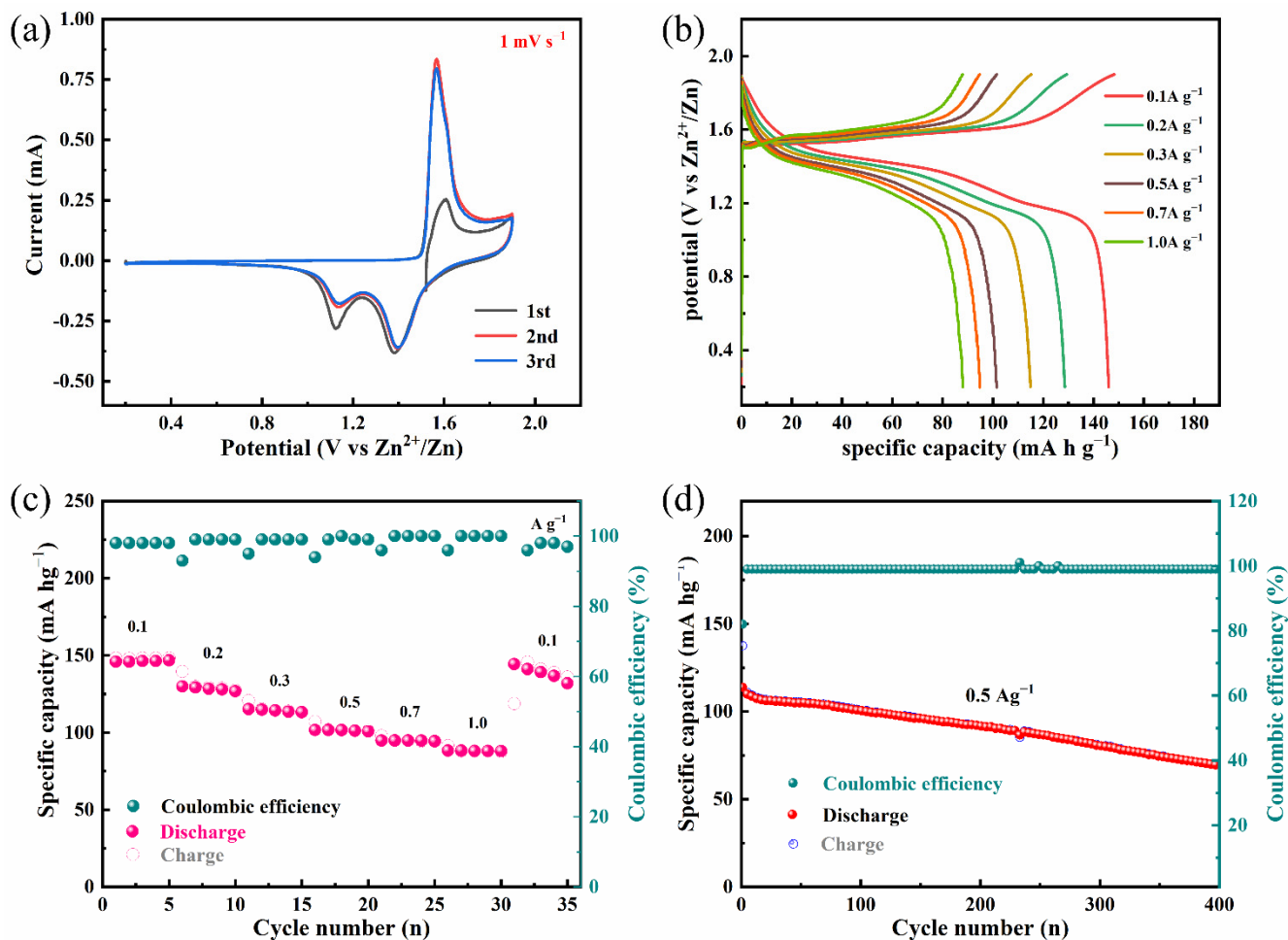


Figure 4. Electrochemical performance of $\text{Mn}(\text{OH})_2//\text{Zn}$ ZIB in coin cells. (a) CV curves scanned at 1 mV s^{-1} . (b) GCD curves tested at various current densities (0.1 – 1.0 Ag^{-1}). (c) Rate performance detected at various specific currents from 0.1 to 1.0 Ag^{-1} . (d) Cycling stability of the $\text{Mn}(\text{OH})_2//\text{Zn}$ coin cells cycled at 0.5 Ag^{-1} .

In order to understand the Zn^{2+} storage behaviors of $\text{Mn}(\text{OH})_2$ nanowire arrays in ZIBs step by step, it is necessary to further investigate the electrochemical kinetics of the sample. A series of tests were performed to quantitatively distinguish the diffusion contribution and the surface capacitance contribution of the product. Figure 5a shows the CV curves at different scan rates from 0.1 to 1 mV s^{-1} under a voltage window of 0.2 – 1.9 V . The measured CV curves have similar shapes. As the scan rate increases, the reduction and oxidation peaks slightly shift to the high and low potentials, respectively. For convenience, the redox peaks were marked as peak 1, peak 2 and peak 3, as shown in Figure 5a. According to the previous studies [43–46], ion electrochemical reaction kinetics can be decided by the relationship of peak current (i) and scan rate (v), as described below:

$$i = av^b$$

here i and v represent the peak current and the scan rate, respectively. The constants a and b are empirical parameters. From the linear relationship between $\log(i)$ and $\log(v)$, one can estimate the value of b . In particular, the b value can offer a critical insight into the energy storage mechanism; $b = 0.5$ indicates a diffusion-controlled process, while $b = 1$

presents surface capacitive-controlled or pseudocapacitive behavior dominated reaction. As shown in Figure 5b, the b values of peak 1, peak 2 and peak 3 are 0.569, 0.592 and 0.459, respectively, which are closer to 0.5, indicating that the zinc-ion insertion reaction is a process dominated by diffusion restriction. We can also calculate the specific contribution of each part by the equation $i = k_1v + k_2v^{1/2}$. Here, the current at a specific potential is divided into two parts: k_1v represents the capacitive contribution and $k_2v^{1/2}$ represents the diffusion effect. Figure 5c shows the proportion of the capacitance contribution at the scan rate of 0.1 mV s^{-1} , which is calculated to be 35.1%. This reveals that the diffusion dominates the total volume at a low scan rate. In addition, by changing the scan rate from 0.1 to 1 mV s^{-1} , the capacitance contribution proportion increases from 35.1% to 82.3%, as shown in Figure 5d, which indicates that the capacitive effect plays a dominant role at high scan rates.

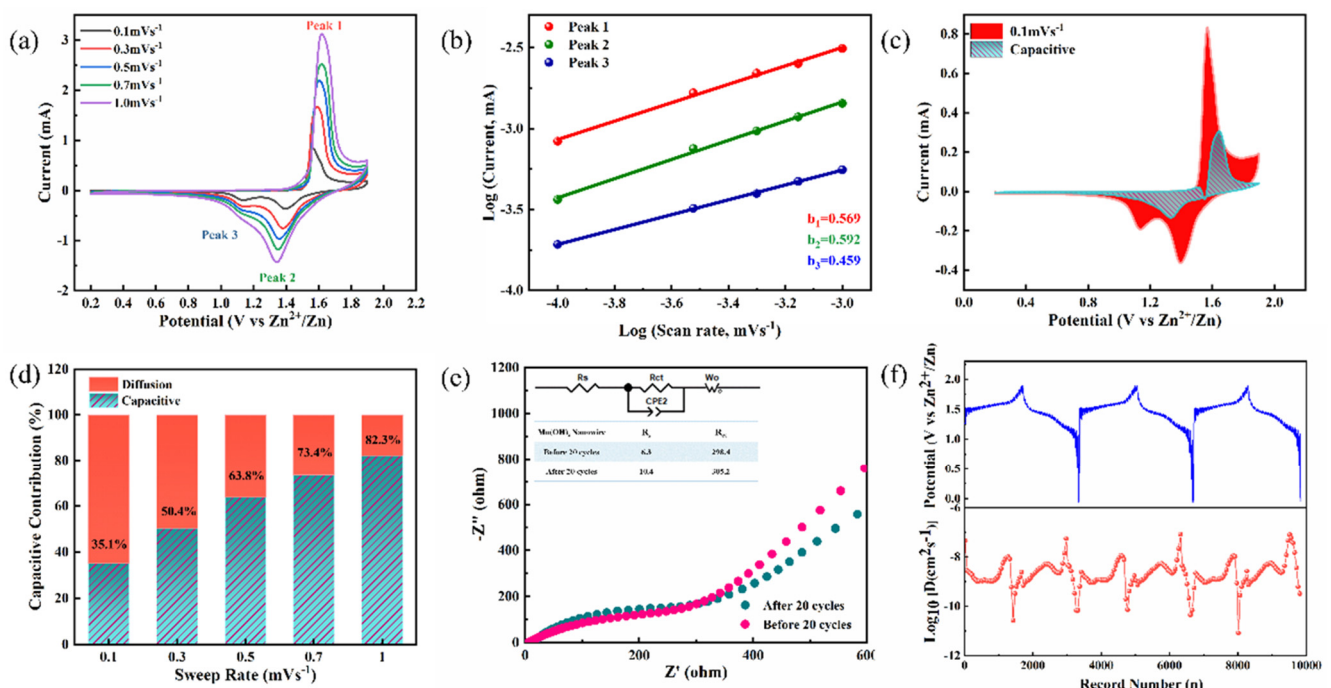


Figure 5. (a) CV curves at different scan rates. (b) $\ln(i)$ versus $\ln(v)$ plots at specific peak currents. (c,d) The contribution ratio of the capacitive capacities and diffusion-limited capacities under different scan rates. (e) Nyquist plot profiles and (f) charge–discharge GITT of $\text{Mn}(\text{OH})_2//\text{Zn}$ ZIB.

To study the resistance and the diffusivity of the sample, the Nyquist diagram and the equivalent circuit are shown in the illustration in Figure 5e. The Z' intercept includes the equivalent series resistance R_s and the resistance of the electrode. The resistance of the $\text{Mn}(\text{OH})_2$ nanowire array is 6.3Ω and 10.4Ω before and after the cycle, indicating that $\text{Mn}(\text{OH})_2$ has a low resistance. The semicircle in the CR2032 battery diagram is related to charge transfer resistance (R_{ct}). The value of R_{ct} after circulation reduces slightly, compared to that before circulation (298.4Ω vs. 305.2Ω), indicating that the insertion of Zn^{2+} activates the material and the electrode has good contact with the electrolyte interface. It can be concluded that the $\text{Mn}(\text{OH})_2$ nanowire array has a low charge transfer resistance, resulting in good rate and electrochemical performances. To further investigate the original charge transfer kinetics, the Nyquist diagrams collected before and after cycles are shown in Figure 5e. Two features are evident: a semicircle in the mid–high frequency region and a steep straight line in the low-frequency region. The impedance data can be fitted according to the equivalent circuit inserted in Figure 5e; the parameters R_s , R_{ct} and Z_w represent the series resistance, charge-transfer resistance and Warburg diffusion process. The R_s value slightly increased from 6.3 to 10.4Ω after the cycle, indicating that $\text{Mn}(\text{OH})_2$ has a low resistance. The R_{ct} value slightly decreased from 305.2 to 298.4Ω after cycling;

the results indicate an activation process in the initial several cycles, which originated from the electrolytes soaked into the electrode surface, making the redox reaction on the entire surface easier. While the slope of the straight-line part in the low-frequency region decreased after the cycles, this indicated that the ionic diffusion rate degraded within the electrode, which caused the formation of solid electrolyte interphase (SEI) growth on the electrode's surface. In addition, GITT was employed to study the dynamics of Zn^{2+} ion diffusivity (the calculated details are shown as the Supporting Notes in the Supplementary Materials). As shown in Figure 5f, the diffusion coefficients of $\text{Mn}(\text{OH})_2$ nanowire arrays are $4.5 \times 10^{-8} \sim 1.0 \times 10^{-9} \text{ cm}^2 \text{ s}^{-1}$ and $1.0 \times 10^{-9} \sim 2.7 \times 10^{-11} \text{ cm}^2 \text{ s}^{-1}$ for charging and discharging processes, respectively, reflecting the rapid ionic diffusion kinetics. Compared with other referenced cathode materials (Table S1), the diffusion coefficients of $\text{Mn}(\text{OH})_2$ nanowire arrays were higher than the Zn^{2+} ion diffusion coefficient in MnO_2 [16–19,47,48], V_2O_5 [20,21,49–51] and that in other related materials [24,25,52]. The high Zn^{2+} ion diffusion coefficients also benefited from the specific configuration in which the vertically aligned arrangement was beneficial to electron transport and the free space between the nanowires, which can provide more ion-diffusion pathways.

4. Conclusions

In conclusion, binder-free electrode $\text{Mn}(\text{OH})_2$ nanowire arrays were facilely synthesized via electrodeposition. The nanowires were vertically aligned on a carbon cloth. The as-prepared $\text{Mn}(\text{OH})_2$ nanowire arrays were used as cathodes to fabricate high-performance rechargeable aqueous ZIBs. Benefitting from their vertically aligned configuration, the electrons can be transported along the axial direction and the ions can diffuse in the free space between the nanowires. As a result, $\text{Mn}(\text{OH})_2$ nanowire arrays yielded a high specific capacitance of $146.3 \text{ mA h g}^{-1}$ at a current density of 0.5 A g^{-1} . Furthermore, the rechargeable $\text{Zn}/\text{Mn}(\text{OH})_2$ battery presented a good capacity retention of 61.1% of the initial value after 400 cycles. Our study presented an inspiring solution to develop a binder-free electrode through a simple surfactant-assistant electroplate method. This study opens a new avenue to boost the electrochemical kinetics for high-performance aqueous ZIBs.

Supplementary Materials: The following supporting information can be downloaded at: <https://www.mdpi.com/article/10.3390/nano12152514/s1>, Figure S1: Calculation details of GITT; Table S1: Diffusion coefficient of Zn^{2+} in referenced cathode materials.

Author Contributions: Conceptualization, J.G.; methodology, J.G.; validation, J.G., B.Z. and Z.Z.; formal analysis, B.Z. and Z.Z.; investigation, J.G., B.Z. and Z.Z.; resources, J.G.; data curation, J.G.; writing—original draft preparation, B.Z. and Z.Z.; writing—review and editing, J.G., Q.D., C.T. and X.W.; visualization, J.G.; supervision, C.T. and X.W.; project administration, J.G.; funding acquisition, J.G. and Y.X. All authors have read and agreed to the published version of the manuscript.

Funding: This work was financially assisted by the National Natural Science Foundation of China (No. 22075068) and Fundamental Research Funds for the Central Universities (No. 2013/B210202149). Work at the Ames was supported by the Department of Energy, Division of Materials Sciences & Engineering (No. DE-AC02-07CH11358).

Institutional Review Board Statement: Not applicable.

Informed Consent Statement: Not applicable.

Data Availability Statement: Not applicable.

Conflicts of Interest: The manuscript was written through the contributions of all authors. All authors have given approval to the final version of the manuscript. The authors declare no competing financial interests.

References

1. Li, M.; Lu, J.; Chen, Z.; Amine, K. 30 Years of Lithium-Ion Batteries. *Adv. Mater.* **2018**, *30*, 1800561. [[CrossRef](#)] [[PubMed](#)]
2. Feng, X.; Ouyang, M.; Liu, X.; Lu, L.; Xia, Y.; He, X. Thermal runaway mechanism of lithium ion battery for electric vehicles: A review. *Energy Stor. Mater.* **2018**, *10*, 246–267. [[CrossRef](#)]

3. Zubi, G.; Dufo-Lopez, R.; Carvalho, M.; Pasaoglu, G. The lithium-ion battery: State of the art and future perspectives. *Renew. Sust. Energ. Rev.* **2018**, *89*, 292–308. [[CrossRef](#)]
4. Nayak, P.K.; Yang, L.; Brehm, W.; Adelhelm, P. From Lithium-Ion to Sodium-Ion Batteries: Advantages, Challenges, and Surprises. *Angew. Chem. Int. Ed.* **2018**, *57*, 102–120. [[CrossRef](#)] [[PubMed](#)]
5. Tang, B.; Shan, L.; Liang, S.; Zhou, J. Issues and opportunities facing aqueous zinc-ion batteries. *Energy Environ. Sci.* **2019**, *12*, 3288–3304. [[CrossRef](#)]
6. Huang, J.; Wang, Z.; Hou, M.; Dong, X.; Liu, Y.; Wang, Y.; Xia, Y. Polyaniline-intercalated manganese dioxide nanolayers as a high-performance cathode material for an aqueous zinc-ion battery. *Nat. Commun.* **2018**, *9*, 2906. [[CrossRef](#)]
7. Fang, G.; Zhou, J.; Pan, A.; Liang, S. Recent Advances in Aqueous Zinc-Ion Batteries. *ACS Energy Lett.* **2018**, *3*, 2480–2501. [[CrossRef](#)]
8. Vo Pham Hoang, H.; Yong Nam, A.; Hur, J. Recent Advances in Transition Metal Dichalcogenide Cathode Materials for Aqueous Rechargeable Multivalent Metal-Ion Batteries. *Nanomaterials* **2021**, *11*, 1517. [[CrossRef](#)]
9. Liu, Y.; Hu, J.; Lu, Q.; Hantusch, M.; Zhang, H.; Qu, Z.; Tang, H.; Dong, H.; Schmidt, O.G.; Holze, R.; et al. Highly enhanced reversibility of a Zn anode by in-situ texturing. *Energy Stor. Mater.* **2022**, *47*, 98–104. [[CrossRef](#)]
10. Lu, Q.; Liu, C.; Du, Y.; Wang, X.; Ding, L.; Omar, A.; Mikhailova, D. Uniform Zn Deposition Achieved by Ag Coating for Improved Aqueous Zinc-Ion Batteries. *ACS Appl. Mater. Interfaces* **2021**, *13*, 16869–16875. [[CrossRef](#)]
11. Cao, X.; Xia, H.; Zhao, X. Toward dendrite-free alkaline zinc-based rechargeable batteries: A minireview. *Funct. Mater. Lett.* **2019**, *12*, 1930004. [[CrossRef](#)]
12. Gao, X.; Li, H.; Cao, X.; Lu, X. Mn₃O₄@MnS composite nanoparticles as cathode materials for aqueous rechargeable Zn ion batteries. *Funct. Mater. Lett.* **2021**, *14*, 2143002. [[CrossRef](#)]
13. Qiu, W.; Li, Y.; You, A.; Zhang, Z.; Li, G.; Lu, X.; Tong, Y. High-performance flexible quasi-solid-state Zn-MnO₂ battery based on MnO₂ nanorod arrays coated 3D porous nitrogen-doped carbon cloth. *J. Mater. Chem. A* **2017**, *5*, 14838–14846. [[CrossRef](#)]
14. Wu, B.; Zhang, G.; Yan, M.; Xiong, T.; He, P.; He, L.; Xu, X.; Mai, L. Graphene Scroll-Coated alpha-MnO₂ Nanowires as High-Performance Cathode Materials for Aqueous Zn-Ion Battery. *Small* **2018**, *14*, 1703850. [[CrossRef](#)] [[PubMed](#)]
15. Chao, D.; Zhou, W.; Ye, C.; Zhang, Q.; Chen, Y.; Gu, L.; Davey, K.; Qiao, S.-Z. An Electrolytic Zn-MnO₂ Battery for High-Voltage and Scalable Energy Storage. *Angew. Chem. Int. Ed.* **2019**, *58*, 7823–7828. [[CrossRef](#)] [[PubMed](#)]
16. Lian, S.; Sun, C.; Xu, W.; Huo, W.; Luo, Y.; Zhao, K.; Yao, G.; Xu, W.; Zhang, Y.; Li, Z.; et al. Built-in oriented electric field facilitating durable Zn-MnO₂ battery. *Nano Energy* **2019**, *62*, 79–84. [[CrossRef](#)]
17. Wu, Y.; Tao, Y.; Zhang, X.; Zhang, K.; Chen, S.; Liu, Y.; Ding, Y.; Cai, M.; Liu, X.; Dai, S. Self-assembled alpha-MnO₂ urchin-like microspheres as a high-performance cathode for aqueous Zn-ion batteries. *Sci. China Mater.* **2020**, *63*, 1196–1204. [[CrossRef](#)]
18. Wang, Y.; Ye, F.; Wu, Z.; Jiang, L.; Zhang, L.; Hu, L. Macroporous, Freestanding Birnessite H_{0.08}MnO₂ center dot 0.7H₂O Nanobelts/Carbon Nanotube Membranes for Wearable Zinc-Ion Batteries with Superior Rate Capability and Cyclability. *ACS Appl. Energy Mater.* **2021**, *4*, 4138–4149. [[CrossRef](#)]
19. Zhang, Y.; Liu, Y.; Liu, Z.; Wu, X.; Wen, Y.; Chen, H.; Ni, X.; Liu, G.; Huang, J.; Peng, S. MnO₂ cathode materials with the improved stability via nitrogen doping for aqueous zinc-ion batteries. *J. Energy Chem.* **2022**, *64*, 23–32. [[CrossRef](#)]
20. Mao, F.; Li, Y.; Zou, Z.; Huang, B.; Yang, J.; Yao, J. Zn²⁺ storage performance and structural change of orthorhombic V₂O₅ nanowires as the cathode material for rechargeable aqueous zinc-ion batteries. *Electrochim. Acta* **2021**, *397*, 139255. [[CrossRef](#)]
21. Li, J.; McColl, K.; Lu, X.; Sathasivam, S.; Dong, H.; Kang, L.; Li, Z.; Zhao, S.; Kafizas, A.G.; Wang, R.; et al. Multi-Scale Investigations of delta-Ni_{0.25}V₂O₅ center dot nH₂O Cathode Materials in Aqueous Zinc-Ion Batteries. *Adv. Energy Mater.* **2020**, *10*, 2000058. [[CrossRef](#)]
22. Du, Y.-H.; Liu, X.-Y.; Wang, X.-Y.; Sun, J.-C.; Lu, Q.-Q.; Wang, J.-Z.; Omar, A.; Mikhailova, D. Freestanding strontium vanadate/carbon nanotube films for long-life aqueous zinc-ion batteries. *Rare Metals* **2022**, *41*, 415–424. [[CrossRef](#)]
23. Chen, Y.; Yin, X.; Lei, S.; Dai, X.; Xu, X.; Shi, W.; Liu, W.; Wu, F.; Cao, X. MXene for aqueous zinc-based energy storage devices. *Funct. Mater. Lett.* **2021**, *14*, 2130011. [[CrossRef](#)]
24. Sha, D.; Lu, C.; He, W.; Ding, J.; Zhang, H.; Bao, Z.; Cao, X.; Fan, J.; Dou, Y.; Pan, L.; et al. Surface Selenization Strategy for V₂CT_x MXene toward Superior Zn-Ion Storage. *ACS Nano* **2022**, *16*, 2711–2720. [[CrossRef](#)] [[PubMed](#)]
25. Gong, J.; Li, H.; Zhang, K.; Zhang, Z.; Cao, J.; Shao, Z.; Tang, C.; Fu, S.; Wang, Q.; Wu, X. Zinc-Ion Storage Mechanism of Polyaniline for Rechargeable Aqueous Zinc-Ion Batteries. *Nanomaterials* **2022**, *12*, 1438. [[CrossRef](#)]
26. Zeng, Y.; Zhang, X.; Meng, Y.; Yu, M.; Yi, J.; Wu, Y.; Lu, X.; Tong, Y. Achieving Ultrahigh Energy Density and Long Durability in a Flexible Rechargeable Quasi-Solid-State Zn-MnO₂ Battery. *Adv. Mater.* **2017**, *29*, 1700274. [[CrossRef](#)]
27. Xu, C.; Li, B.; Du, H.; Kang, F. Energetic Zinc Ion Chemistry: The Rechargeable Zinc Ion Battery. *Angew. Chem. Int. Ed.* **2012**, *51*, 933–935. [[CrossRef](#)]
28. Guo, X.; Zhou, J.; Bai, C.; Li, X.; Fang, G.; Liang, S. Zn/MnO₂ battery chemistry with dissolution-deposition mechanism. *Mater. Today Energy* **2020**, *16*, 100396. [[CrossRef](#)]
29. Pan, H.; Shao, Y.; Yan, P.; Cheng, Y.; Han, K.S.; Nie, Z.; Wang, C.; Yang, J.; Li, X.; Bhattacharya, P.; et al. Reversible aqueous zinc/manganese oxide energy storage from conversion reactions. *Nat. Energy* **2016**, *1*, 16039. [[CrossRef](#)]
30. Zhang, Y.; Dong, X.; Li, H.; Cui, C.; Fu, C.; Zeng, S.; Wang, L. A controlled synthesis of gamma-MnOOH nanorods via a facile hydrothermal method for high-performance Li-ion batteries. *CrystEngComm* **2021**, *23*, 2376–2383. [[CrossRef](#)]

31. Zhang, Z.; Tang, C.; Zhang, K.; Li, H.; Cao, J.; Shao, Z.; Gong, J. Synthesis of Mn(OH)₂ Nanosheets on Carbon Cloth for High-Performance Aqueous Zinc-Ion Battery. *J. Nanoelectron. Optoe.* **2021**, *16*, 1698–1704. [[CrossRef](#)]
32. Yang, Z.; Gong, J.; Tang, C.; Zhu, W.; Cheng, Z.; Jiang, J.; Ma, A.; Ding, Q. Vertically-aligned Mn(OH)₂ nanosheet films for flexible all-solid-state electrochemical supercapacitors. *J. Mater. Sci. Mater. Electron.* **2017**, *28*, 17533–17540. [[CrossRef](#)]
33. Wang, M.; Liu, X.; Liu, H.; Zhao, D.; Wu, X. NiCo layered double hydroxide nanosheets with enhanced electrochemical performance. *J. Alloys Compd.* **2022**, *903*, 163926. [[CrossRef](#)]
34. Li, J.-C.; Gong, J.; Zhang, X.; Lu, L.; Liu, F.; Dai, Z.; Wang, Q.-J.; Hong, X.; Pang, H.; Han, M. Alternate Integration of Vertically Oriented CuSe@FeOOH and CuSe@MnOOH Hybrid Nanosheets Frameworks for Flexible In-Plane Asymmetric Micro-supercapacitors. *ACS Appl. Energy Mater.* **2020**, *3*, 3692–3703. [[CrossRef](#)]
35. Gong, J.; Tian, Y.; Yang, Z.; Wang, Q.; Hong, X.; Ding, Q. High-Performance Flexible All-Solid-State Asymmetric Supercapacitors Based on Vertically Aligned CuSe@Co(OH)₂ Nanosheet Arrays. *J. Phys. Chem. C* **2018**, *122*, 2002–2011. [[CrossRef](#)]
36. Gong, J.; Li, J.-C.; Yang, J.; Zhao, S.; Yang, Z.; Zhang, K.; Bao, J.; Pang, H.; Han, M. High-Performance Flexible In-Plane Micro-Supercapacitors Based on Vertically Aligned CuSe@Ni(OH)₂ Hybrid Nanosheet Films. *ACS Appl. Mater. Interfaces* **2018**, *10*, 38341–38349. [[CrossRef](#)]
37. Guo, X.; Li, J.; Jin, X.; Han, Y.; Lin, Y.; Lei, Z.; Wang, S.; Qin, L.; Jiao, S.; Cao, R. A Hollow-Structured Manganese Oxide Cathode for Stable Zn-MnO₂ Batteries. *Nanomaterials* **2018**, *8*, 301. [[CrossRef](#)]
38. Xu, G.-R.; Xie, C.-P.; Wen, Y.; Tang, A.-P.; Song, H.-S. Mn(OH)₂ electrodeposited on secondary porous Ni nano-architecture foam as high-performance electrode for supercapacitors. *Ionics* **2019**, *25*, 3287–3298. [[CrossRef](#)]
39. Nesbitt, H.W.; Banerjee, D. Interpretation of XPS Mn(2p) spectra of Mn oxyhydroxides and constraints on the mechanism of MnO₂ precipitation. *Am. Mineral.* **1998**, *83*, 305–315. [[CrossRef](#)]
40. Anandan, S.; Gnana Sundara Raj, B.; Lee, G.-J.; Wu, J.J. Sonochemical synthesis of manganese (II) hydroxide for supercapacitor applications. *Mater. Res. Bull.* **2013**, *48*, 3357–3361. [[CrossRef](#)]
41. Jia, D.; Li, Q.; Hanna, K.; Mailhot, G.; Brigante, M. Efficient removal of estrogenic compounds in water by MnIII-activated peroxymonosulfate: Mechanisms and application in sewage treatment plant water. *Environ. Pollut.* **2021**, *288*, 117728. [[CrossRef](#)] [[PubMed](#)]
42. Ilton, E.S.; Post, J.E.; Heaney, P.J.; Ling, F.T.; Kerisit, S.N. XPS determination of Mn oxidation states in Mn (hydr)oxides. *Appl. Surf. Sci.* **2016**, *366*, 475–485. [[CrossRef](#)]
43. Kim, H.-S.; Cook, J.B.; Lin, H.; Ko, J.S.; Tolbert, S.H.; Ozolins, V.; Dunn, B. Oxygen vacancies enhance pseudocapacitive charge storage properties of MoO_{3-x}. *Nat. Mater.* **2017**, *16*, 454. [[CrossRef](#)] [[PubMed](#)]
44. Chao, D.; Zhu, C.; Yang, P.; Xia, X.; Liu, J.; Wang, J.; Fan, X.; Savilov, S.V.; Lin, J.; Fan, H.J.; et al. Array of nanosheets render ultrafast and high-capacity Na-ion storage by tunable pseudocapacitance. *Nat. Commun.* **2016**, *7*, 12122. [[CrossRef](#)] [[PubMed](#)]
45. Gong, M.; Zhou, W.; Tsai, M.-C.; Zhou, J.; Guan, M.; Lin, M.-C.; Zhang, B.; Hu, Y.; Wang, D.-Y.; Yang, J.; et al. Nanoscale nickel oxide/nickel heterostructures for active hydrogen evolution electrocatalysis. *Nat. Commun.* **2014**, *5*, 4695. [[CrossRef](#)]
46. Yang, Y.; Zheng, G.; Cui, Y. Nanostructured sulfur cathodes. *Chem. Soc. Rev.* **2013**, *42*, 3018–3032. [[CrossRef](#)]
47. Guo, C.; Liu, H.; Li, J.; Hou, Z.; Liang, J.; Zhou, J.; Zhu, Y.; Qian, Y. Ultrathin delta-MnO₂ nanosheets as cathode for aqueous rechargeable zinc ion battery. *Electrochim. Acta* **2019**, *304*, 370–377. [[CrossRef](#)]
48. Xu, J.-W.; Gao, Q.-L.; Xia, Y.-M.; Lin, X.-S.; Liu, W.-L.; Ren, M.-M.; Kong, F.-G.; Wang, S.-J.; Lin, C. High-performance reversible aqueous zinc-ion battery based on iron-doped alpha-manganese dioxide coated by polypyrrole. *J. Colloid Interface Sci.* **2021**, *598*, 419–429. [[CrossRef](#)]
49. Liu, Y.; Liu, Y.; Wu, X.; Cho, Y.-R. Enhanced Electrochemical Performance of Zn/VO_x Batteries by a Carbon-Encapsulation Strategy. *ACS Appl. Mater. Interfaces* **2022**, *14*, 11654–11662. [[CrossRef](#)]
50. Wang, M.; Zhang, J.; Zhang, L.; Li, J.; Wang, W.; Yang, Z.; Zhang, L.; Wang, Y.; Chen, J.; Huang, Y.; et al. Graphene-like Vanadium Oxygen Hydrate (VOH) Nanosheets Intercalated and Exfoliated by Polyaniline (PANI) for Aqueous Zinc-Ion Batteries (ZIBs). *ACS Appl. Mater. Interfaces* **2020**, *12*, 31564–31574. [[CrossRef](#)]
51. Liu, X.; Ma, L.; Du, Y.; Lu, Q.; Yang, A.; Wang, X. Vanadium Pentoxide Nanofibers/Carbon Nanotubes Hybrid Film for High-Performance Aqueous Zinc-Ion Batteries. *Nanomaterials* **2021**, *11*, 1054. [[CrossRef](#)] [[PubMed](#)]
52. Liu, X.; Shen, X.; Chen, T.; Xu, Q. The spinel MnFe₂O₄ grown in biomass-derived porous carbons materials for high-performance cathode materials of aqueous zinc-ion batteries. *J. Alloys Compd.* **2022**, *904*, 164002. [[CrossRef](#)]